

Adaptive Imaging of Arbitrary Thermal Source Distributions with Near Quantum-Limited Resolution

Erik F. Matlin and Lucas J. Zipp

Advanced Technology and Sciences Division, SRI International, Menlo Park, California 94025, USA

(Dated: June 28, 2021)

We demonstrate an approach to obtaining near quantum limited far-field imaging resolution of thermal, incoherent sources with arbitrary distributions. Our method assumes no prior knowledge of the source distribution, but rather uses an adaptive approach to imaging via spatial-mode demultiplexing that iteratively updates both the form of the spatial imaging modes and the estimate of the source distribution. The optimal imaging modes are determined by minimizing the estimated Cramér-Rao bound over the manifold of all possible sets of orthogonal modes. We have observed through Monte Carlo simulations that the manifold-optimized spatial mode demultiplexing measurement consistently outperforms standard imaging techniques in the resolution and precision of source reconstructions, and approaches the quantum limits as set by the quantum Cramér-Rao bound. The adaptive framework presented here allows for a consistent approach to achieving near quantum-limited imaging resolution of arbitrarily distributed thermal sources.

Advances in super-resolution imaging methods in the field of fluorescence microscopy [1–3], as well as techniques that leverage the use of quantum, non-classical light sources [4, 5] have demonstrated the ability to surpass the classical diffraction limit. However, these techniques require either active illumination or special sample preparation and are therefore not applicable to passive far-field imaging scenarios. As a result, the resolution limit of standard far-field imaging has remained constrained by the classical diffraction limit, as embodied by the well-known Rayleigh criterion.

Recently, it was shown that the traditional method of far-field imaging, (i.e., detecting photons in the position basis in the image plane) which we will refer to as direct imaging, falls significantly short of the quantum limit of resolution when estimating the separation of two incoherent point sources [6]. Instead, the quantum limit is achieved by projecting the light field onto a set of orthogonal spatial modes before detection, sometimes referred to as spatial-mode demultiplexing imaging (SPADE). Subsequent work, both theoretical and experimental, has confirmed this approach for achieving quantum-limited separation estimation of two point sources [7–14], with experimental realizations of SPADE imaging using interferometers [12] or digital holography techniques [13, 14].

Progress has been made in generalizing these techniques to multiple point sources or extended sources [15–21], as well as to adaptive methods [22, 23], but no practical framework has been developed for achieving quantum-limited resolution in the case of arbitrary incoherent source distributions, with no prior information about the distribution assumed. This is due to the seemingly daunting challenge of minimizing the Cramér-Rao bound (CRB) for arbitrary sources as the number of parameters tends towards infinity [24].

In this work, we demonstrate an adaptive method for achieving optimal quantum-limited resolution of ther-

mal sources based on optimizing the spatial imaging modes over the manifold of orthonormal functions, which we term manifold-optimized spatial-mode demultiplexing (MO-SPADE). The method provides an increase in the fundamental resolution of the imaging system, with performance that approaches the quantum limit as set by the quantum Cramér-Rao bound (QCRB). In contrast to super-resolution techniques that apply post-processing to achieve sharper image reconstructions [25, 26], the measurement method described in this work fundamentally increases the amount of information available on the source distribution.

Optimal Imaging Methodology. The setup of the adaptive spatial mode imager, shown in Fig. 1, consists of a two-dimensional thermal source region $F(\mathbf{R})$ emitting spatially incoherent light which is imaged in the far-field through a hard aperture. At the image plane, the field is sorted into a set of orthonormal spatial modes $\Phi = \{\phi_j(\mathbf{r})|j = 0, \dots, J-1\}$, and measured by individual photon counting detectors. We assume a weak thermal source such that less than one photon is detected within a coherence time interval, and the detection events can be modeled as a Poisson process [6]. The photon counts in each channel are then used to reconstruct a source estimate, as well as to update the optimal set of imaging spatial modes for the next measurement iteration.

To optimize the imaging for arbitrary incoherent source distributions, we parametrize the source by decomposing it into a set of orthogonal functions:

$$F(\mathbf{R}) = \sum_k c_k f_k(\mathbf{R}), \quad (1)$$

where $F(\mathbf{R})$ is the source brightness in the object plane, and $f_k(\mathbf{R})$ is the k_{th} function in the source decomposition basis set. We will refer to these functions as source modes, to distinguish them from the spatial imaging modes. To make the problem computationally tractable we restrict the number of source modes to a finite value

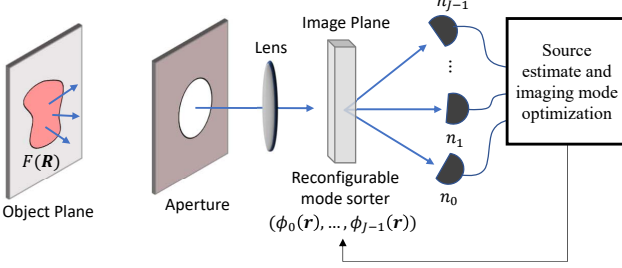


FIG. 1. Adaptive spatial-mode imaging system. Light from the far-field source distribution $F(\mathbf{R})$ is captured by a hard aperture and imaged onto a spatial mode sorter of imaging modes Φ . At each measurement iteration, the number of photons detected in each channel n_j is used to generate a source estimate, as well as an updated set of optimal spatial imaging modes for the next measurement iteration.

K , such that $F(\mathbf{R})$ can be adequately approximated in its subspace. The imaging problem then becomes one of accurately estimating the multiparameter coefficient vector $\mathbf{c} = (c_1, c_2, \dots, c_K)$ in the presence of noise. We restrict our attention to the case where the imaging noise is dominated by the photon shot noise and other noise sources are negligible, as is often the case for photon detection in the visible spectrum. To properly frame this measurement problem, we use the statistical tools of the Fisher information matrix and the corresponding Cramér-Rao bound, which sets the lowest achievable mean squared error (MSE) of the coefficient estimates of any unbiased estimator. The classical Fisher information per photon measured with the orthonormal imaging modes Φ is constructed as [6]

$$\mathcal{I}(\mathbf{c}; \Phi)_{kl} = \sum_{j=1}^J \frac{1}{P_j} \left(\frac{\partial P_j}{\partial c_k} \right) \left(\frac{\partial P_j}{\partial c_l} \right), \quad (2)$$

where P_j is the probability, conditioned on a detection event, of detecting a photon in imaging mode ϕ_j . For incoherent source distributions this probability is given by

$$P_j = \int d\mathbf{R} F(\mathbf{R}) |\langle \phi_j | \psi_{\mathbf{R}}^{PSF} \rangle|^2, \quad (3)$$

where $|\psi_{\mathbf{R}}^{PSF}\rangle$ is the field point spread function (PSF) in the image plane originating from source point \mathbf{R} . Replacing $F(\mathbf{R})$ with its orthogonal decomposition allows us to directly evaluate the partial derivative terms. The covariance matrix of the coefficient vector for any unbiased estimator satisfies the inequality

$$\text{cov}(\mathbf{c}) \geq [\mathcal{I}(\mathbf{c}; \Phi)]^{-1} \quad (4)$$

known as the Cramér-Rao bound. Specifically, the MSE of any unbiased estimator of the coefficient c_k is bounded

by the corresponding diagonal entry of the Fisher information matrix inverse:

$$\text{MSE}(c_k) > [\mathcal{I}(\mathbf{c}; \Phi)]_{kk}^{-1} \quad (5)$$

The optimal imaging problem can then be cast into one of minimizing the MSE of the source coefficients by minimizing the diagonal elements of the Fisher information matrix inverse. The objective function to be minimized is

$$L(\Phi) = \text{tr} (W[\mathcal{I}(\mathbf{c}; \Phi)]^{-1}), \quad (6)$$

where W is a weighting matrix that can be applied depending on the nature of the imaging task. In the results shown here, we choose W to be equal to the identity matrix, corresponding to minimizing the Cramér-Rao bound averaged over all source coefficients c_k . The objective function $L(\Phi)$ is minimized over the manifold of all possible orthonormal imaging modes using numerical manifold optimization methods [27]. Our specific implementation uses the Scaled Gradient Projection Method (SGPM) designed for the minimization of functions over the set of orthonormal matrices, known as a Stiefel manifold [28].

Optimized imaging of point sources and extended sources. Before demonstrating the full adaptive imaging method, we first characterize the maximum imaging improvement attainable assuming the true source distribution is known for the purposes of computing the Fisher information matrix in Eq. (2). We first apply the MO-SPADE imaging method to one-dimensional imaging of a line of incoherent point sources, where the locations of the sources are known a priori and the task is to estimate the magnitudes of the point sources. This scenario applies, for instance, in estimating the brightness of closely spaced astronomical objects whose locations are known from other indirect methods. The source modes are then Dirac delta functions located at the point sources. For simplicity we assume a shift-invariant Gaussian field PSF of $\psi_R^{PSF}(x) = (2\pi\sigma^2)^{-1/4} \exp[-(x - R)^2 / (4\sigma^2)]$ and we have normalized the image plane spatial coordinate x by the magnification factor of the imaging system. The width σ of the Gaussian PSF is approximately related to the radius r_c of a corresponding Airy disk by $\sigma \approx r_c/3$ [29].

Figure 2(a-d) displays the results of MO-SPADE imaging of five equally spaced point sources using mode sorting detection with five spatial imaging modes. We find that for point source spacings Δx in the sub-Rayleigh regime, MO-SPADE imaging attains a lower CRB compared to direct imaging, with an advantage that grows larger as $\Delta x \rightarrow 0$. In terms of resolution, MO-SPADE allows for smaller Δx point source spacings before reaching the equivalent CRB value of direct imaging, showing an increase in effective resolution by over a factor of 1.5 in the deep sub-Rayleigh regime. The spatial imaging modes which attain this performance are shown in

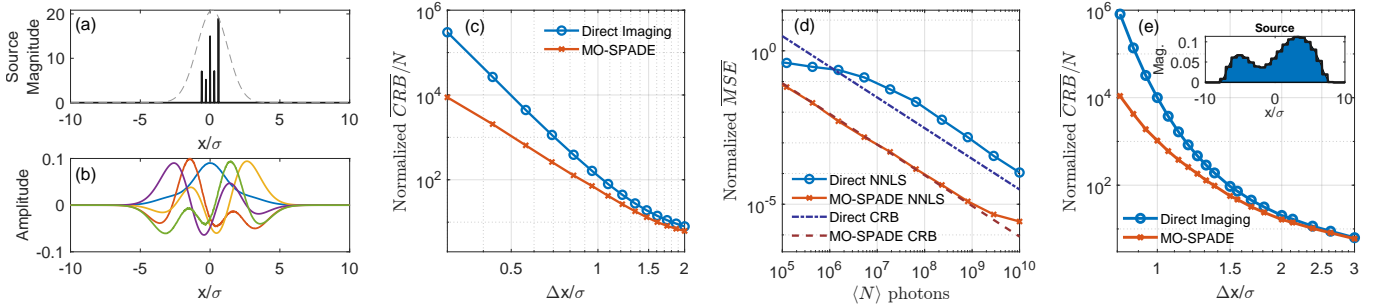


FIG. 2. Demonstration of MO-SPADE imaging on point sources and extended sources. (a) Source distribution of 5 equidistant point sources, shown here for a separation of $\Delta x = 0.3\sigma$. The dashed curve shows the outline of the PSF-convolved distribution in the image plane. (b) The manifold-optimized spatial imaging modes for the point source distribution. (c) The CRB averaged over all point source magnitude coefficients plotted at various point source separations. (d) Results of the Monte Carlo simulations for a point source separation of $\Delta x = 0.3\sigma$. Each data point represents the MSE of 100 trials averaged over all point source magnitudes. (e) Demonstration of MO-SPADE imaging for extended sources. The CRB averaged over all source magnitude coefficients is shown for various source mode rectangle widths. Smaller widths correspond to a larger number of rectangle functions being used to discretize the source region at a finer resolution. The inset shows the extended source distribution magnitude, with the black outline showing its discretization into rectangle functions with width $a = 0.8\sigma$. The entire discretized source region extends over $\pm 12\sigma$, and $J = K + 1$ imaging modes are used. The CRB and MSE are normalized by the mean of the squared source mode coefficients.

Fig. 2(b). Their profiles are influenced by the source distribution and PSF, and become increasingly complex for larger numbers of imaging modes and sub-Rayleigh source modes. We confirmed the performance enhancement via Monte-Carlo simulations for $\Delta x = 0.3\sigma$, collecting a mean value of $\langle N \rangle$ photons for each trial (Fig. 2(d)). The non-negative least squares (NNLS) estimates of the point source amplitudes follow the CRB limits as expected for large values of $\langle N \rangle$, and confirms that MO-SPADE imaging achieves a factor of 30 reduction in the MSE of the source reconstruction. For low photon numbers, the MSE of the NNLS estimates fall below the CRB due to its nonzero bias.

MO-SPADE imaging also shows enhanced performance when imaging arbitrary extended objects, as shown in Fig. 2(e). The one-dimensional source region is approximately discretized into a set of non-overlapping rectangle functions with width a . We have chosen rectangle functions for simplicity, but other basis choices may be more appropriate depending on the imaging task. The optimization of the spatial imaging modes Φ then proceeds in an identical way as with the point source demonstration. MO-SPADE imaging achieves more than a 10-fold reduction in the CRB of the extended source amplitude estimation in the deep sub-Rayleigh regime, analogous to the point source imaging task. In both of these imaging scenarios, the direct imaging CRB converges towards the optimal CRB for large Δx , in agreement with previous studies on two point sources.

Comparison to quantum limit We can compare our results to the QCRB, which sets a lower bound on the CRB that can be achieved for any possible measurement of a quantum system. We compute the QCRB on an extended source distribution by taking the in-

verse of the quantum Fisher information matrix $\mathcal{K}_{kl} = \text{Re}(\text{tr}[L_k(\rho)L_l(\rho)\rho])$, where $L_k(\rho)$ is the symmetric logarithmic derivative (SLD) of density matrix ρ computed

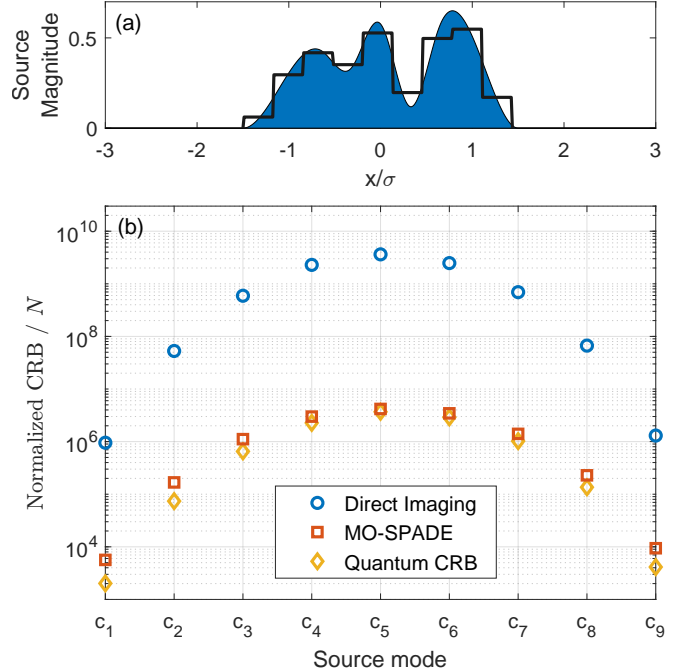


FIG. 3. Comparison to the quantum Cramer-Rao bound. (a) Source distribution discretized into nine rectangle modes. (b) Normalized CRB of the source amplitude coefficients for direct imaging (blue circles), MO-SPADE imaging (red squares), and the quantum CRB limit (yellow diamonds), for a Gaussian PSF with half-width σ .

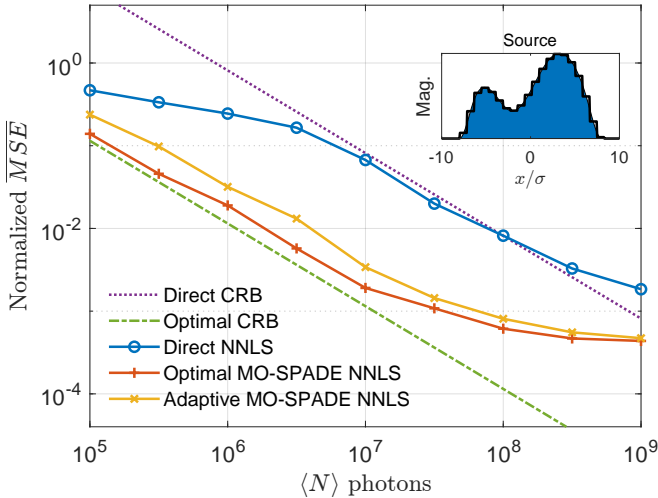


FIG. 4. Monte Carlo simulation of adaptive imaging approach. The normalized MSE over 25 trials of an extended source distribution discretized into rectangles with width $a = 0.8\sigma$ (inset - same as Fig. 2(e)) is plotted for various levels of photons. Note that at high photon levels, the MSE of all methods approaches an error floor due to the discretized approximation of the continuous source.

as [6]:

$$\mathcal{L}_k(\rho) = \sum_{q,p: \lambda_q + \lambda_p \neq 0} \frac{2}{\lambda_q + \lambda_p} \langle e_q | \frac{\partial \rho}{\partial c_k} | e_p \rangle \langle e_q | e_p |, \quad (7)$$

where λ_j and $|e_j\rangle$ are the eigenvalues and eigenvectors of ρ . Details of the computation are provided in the Supplemental Material. Figure 3 compares the QCRB with both the MO-SPADE CRB as well as the direct imaging CRB for an extended source. The MO-SPADE CRB is within a factor of two of the QCRB on average. This is particularly remarkable because the multi-parameter QCRB is a loose lower bound and not guaranteed to be attainable for all parameters simultaneously [30, 31]. By tuning the weight matrix in the optimization objective function, the MO-SPADE CRB of any single parameter can be made to approach arbitrarily close the QCRB limit. This is in agreement with the well-known property that the QCRB of a single-parameter estimation problem can always be attained by forming a positive operator-valued measure (POVM) with the eigenvectors of the SLD [30].

Adaptive imaging on unknown source distributions So far, the CRB and optimal imaging modes have been derived under the assumption of a known source distribution. In most practical cases, the true source distribution is unknown, and it is the purpose of the imaging measurement itself to estimate the source distribution. To solve this problem, an iterative, adaptive approach to imaging is used, where the measurement duration is divided into multiple measurement periods, and the source distribution and optimal MO-SPADE imaging modes are

alternately estimated. At each adaptive iteration i the estimated Fisher information is calculated using the source estimate \mathbf{c}_{i-1}^{est} from the previous iteration along with both previous and current imaging modes, weighted according to the relative number of collected photons N_i ,

$$\mathcal{I}_i^{est} = \sum_{m=1}^i N_m \mathcal{I}(\mathbf{c}_{i-1}^{est}; \Phi_m). \quad (8)$$

The set of orthonormal imaging modes, Φ_i , are optimized by minimizing the estimated CRB: $L(\Phi_i) = \text{tr}(\mathcal{W}[\mathcal{I}_i^{est}]^{-1})$. To initialize the adaptive iterations, we set Φ_0 as the direct imaging basis to take the first measurement. At each iteration, all previous measurement data is used in calculating the estimated source coefficients. By following this iterative scheme, we obtain progressively better estimates of the source distribution, and simultaneously approach the optimal imaging modes for the true source distribution.

To validate the adaptive approach, we performed a Monte Carlo simulation of the reconstruction performance using the NNLS estimator for an arbitrary one-dimensional source and compared it to the performance of both direct imaging and the adaptive optimal imaging as described above. In this simulation, 15% of the measurement duration is spent on the initial direct measurement, and the rest of the duration is split equally among two adaptive MO-SPADE measurements – a configuration that we have empirically found to work well.

The results of this simulation are shown in Fig. 4. At low photon levels, the bias of the NNLS estimator allows the direct imaging MSE to fall below the CRB. As the photon level is increased, the approaches begin to follow the CRB, where this trend continues until the approximation of the source by rectangular modes imposes a floor on the reconstruction error. In the CRB-following region, the adaptive MO-SPADE imaging approach attains a performance that is more than an order of magnitude better than direct imaging and within a small factor of the optimal (prior-knowledge) MO-SPADE imaging.

Finally, we demonstrate the performance of the adaptive imaging on an arbitrary two-dimensional source distribution. For this result, we assume an Airy disk PSF corresponding to imaging through a circular aperture, $\psi_{\mathbf{R}}^{PSF}(r) = (\pi)^{-1/2} J_1(|\mathbf{r} - \mathbf{R}|/\gamma) / |\mathbf{r} - \mathbf{R}|$, where $\gamma = \lambda/(2\pi NA)$, λ is the free-space wavelength, NA is the numerical aperture of the imaging system, and the image plane coordinates are normalized by the magnification factor. Figure 5 shows the results of the adaptive imaging measurement for a source that exhibits varying spatial frequency and contrast. As in the previous one-dimensional demonstration, 15% of the photons were used for the initial direct imaging measurement, and the rest of the photons were divided evenly among two adaptive modal measurements. Comparing the reconstruction results using the NNLS estimator, adaptive MO-SPADE

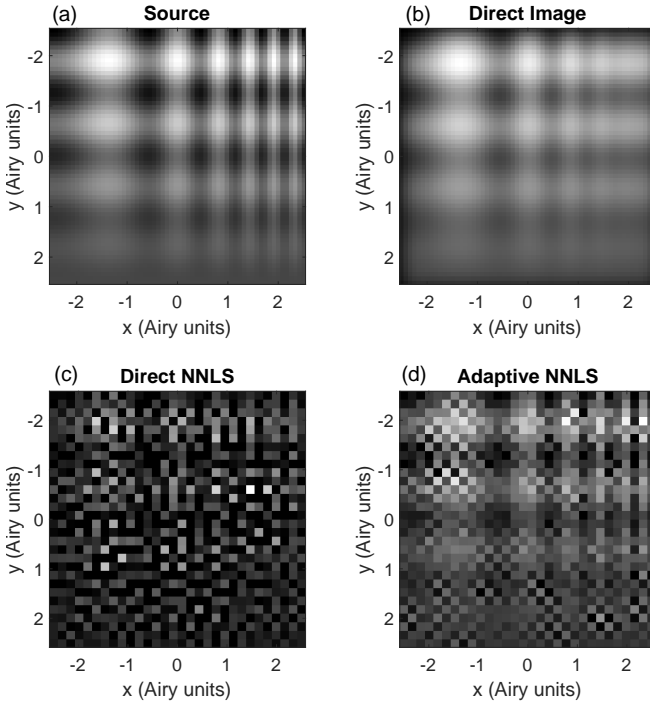


FIG. 5. Example comparison of imaging methods for extended source distributions. The source distribution to be imaged is shown in (a), with corresponding PSF-convolved image-plane intensity distribution shown in (b). A comparison of the NNLS reconstruction results is shown for (c) direct (normalized MSE=0.81) and (d) adaptive MO-SPADE imaging (normalized MSE=0.10) with 10^{10} photons collected. The source is discretized into rectangles with a width of $1/6 \times 1/6$ Airy units, where an Airy unit is equal to the diameter of the Airy disk PSF.

imaging outperforms the direct imaging reconstruction by an order of magnitude in MSE, and is able to resolve features well-below the classical Rayleigh resolution limit. In addition, the MSE of the adaptive MO-SPADE reconstruction is within 30% of the MSE of the optimal MO-SPADE reconstruction (not shown), which uses full prior knowledge of the source distribution for selecting imaging modes.

Conclusion Our results demonstrate a general framework for the imaging of thermal sources with arbitrary distributions at the quantum limits of performance in terms of effective resolution and amplitude estimation error. Further improvements to the adaptive imaging method described here could be made by incorporating the bias of estimators into the optimization framework [32]. This would allow for improved imaging performance with estimators that are biased at low photon numbers, such as NNLS and maximum likelihood estimators (e.g. Richardson-Lucy deconvolution). The adaptive imaging method presented here for incoherent thermal sources can be applied to many fields such as multi-emitter fluorescence microscopy and astronomical imaging, provided

that suitable hardware for the adaptive spatial mode demultiplexing can be developed.

We thank Brian Slovick for valuable comments. This work was funded by the Defense Advanced Research Projects Agency (DARPA) under Agreement No. HR00112090126.

-
- [1] S. W. Hell and J. Wichmann, Opt. Lett. **19**, 780 (1994).
 - [2] S. W. Hell, Science **316**, 1153 (2007).
 - [3] W. E. Moerner, Proceedings of the National Academy of Sciences **104**, 12596 (2007).
 - [4] F. Sciarrino, C. Vitelli, F. De Martini, R. Glasser, H. Cable, and J. P. Dowling, Phys. Rev. A **77**, 012324 (2008).
 - [5] R. Tenne, U. Rossman, B. Rephael, Y. Israel, A. Krupinski-Ptaszek, R. Lapkiewicz, Y. Silberberg, and D. Oron, Nature Photonics **13**, 116 (2019).
 - [6] M. Tsang, R. Nair, and X.-M. Lu, Phys. Rev. X **6**, 031033 (2016).
 - [7] R. Nair and M. Tsang, Phys. Rev. Lett. **117**, 190801 (2016).
 - [8] C. Lupo and S. Pirandola, Phys. Rev. Lett. **117**, 190802 (2016).
 - [9] Z. Yu and S. Prasad, Phys. Rev. Lett. **121**, 180504 (2018).
 - [10] J. Yang, S. Pang, Y. Zhou, and A. N. Jordan, Phys. Rev. A **100**, 032104 (2019).
 - [11] K. Liang, S. A. Wadood, and A. N. Vamivakas, Optica **8**, 243 (2021).
 - [12] W.-K. Tham, H. Ferretti, and A. M. Steinberg, Phys. Rev. Lett. **118**, 070801 (2017).
 - [13] M. Paúr, B. Stoklasa, Z. Hradil, L. L. Sánchez-Soto, and J. Rehacek, Optica **3**, 1144 (2016).
 - [14] Y. Zhou, J. Yang, J. D. Hassett, S. M. H. Rafsanjani, M. Mirhosseini, A. N. Vamivakas, A. N. Jordan, Z. Shi, and R. W. Boyd, Optica **6**, 534 (2019).
 - [15] M. Tsang, New Journal of Physics **19**, 23054 (2017).
 - [16] K. A. G. Bonsma-Fisher, W.-K. Tham, H. Ferretti, and A. M. Steinberg, New Journal of Physics **21**, 093010 (2019).
 - [17] E. Bisketzi, D. Branford, and A. Datta, New Journal of Physics **21**, 123032 (2019).
 - [18] Z. Dutton, R. Kerviche, A. Ashok, and S. Guha, Phys. Rev. A **99**, 033847 (2019).
 - [19] C. Lupo, Z. Huang, and P. Kok, Phys. Rev. Lett. **124**, 080503 (2020).
 - [20] M. E. Pearce, E. T. Campbell, and P. Kok, Quantum **1**, 10.22331/q-2017-07-26-21 (2017), arXiv:1612.04828.
 - [21] L. A. Howard, G. G. Gillett, M. E. Pearce, R. A. Abrahao, T. J. Weinhold, P. Kok, and A. G. White, Phys. Rev. Lett. **123**, 143604 (2019).
 - [22] M. R. Grace, Z. Dutton, A. Ashok, and S. Guha, J. Opt. Soc. Am. A **37**, 1288 (2020).
 - [23] A. Sajjad, M. R. Grace, Q. Zhuang, and S. Guha, Attaining quantum limited precision of localizing an object in passive imaging (2021), arXiv:2102.02228 [quant-ph].
 - [24] M. Tsang, Phys. Rev. Research **1**, 033006 (2019).
 - [25] E. Nehme, L. E. Weiss, T. Michaeli, and Y. Shechtman, Optica **5**, 458 (2018).
 - [26] H. Wang, Y. Rivenson, Y. Jin, Z. Wei, R. Gao, H. Günaydin, L. A. Bentolila, C. Kural, and A. Ozcan,

- Nature Methods **16**, 103 (2019).
- [27] J. Hu, X. Liu, Z.-W. Wen, and Y.-X. Yuan, Journal of the Operations Research Society of China **8**, 199 (2020).
- [28] H. Oviedo and O. Dalmau, in *Advances in Soft Computing*, edited by L. Martínez-Villaseñor, I. Batyrshin, and A. Marín-Hernández (Springer International Publishing, Cham, 2019) pp. 239–250.
- [29] B. Zhang, J. Zerubia, and J.-C. Olivo-Marin, Appl. Opt. **46**, 1819 (2007).
- [30] F. Albarelli, M. Barbieri, M. G. Genoni, and I. Gianani, Physics Letters A **384**, 126311 (2020).
- [31] J. Liu, H. Yuan, X.-M. Lu, and X. Wang, Journal of Physics A: Mathematical and Theoretical **53**, 023001 (2019).
- [32] M. Tsang, Journal of Modern Optics **65**, 1385 (2018).